MATERIALS SCIENCE

Improper molecular ferroelectrics with simultaneous ultrahigh pyroelectricity and figures of merit

Wenru Li[1]*, Gang Tang[2]*, Guangzu Zhang[1†], Hasnain Mehdi Jafri[3], Jun Zhou[1], Di Liu[3], Yang Liu[4], Jiesu Wang[5], Kuijuan Jin[5], Yongmin Hu[6], Haoshuang Gu[6], Zhao Wang[6], Jiawang Hong[2†], Houbing Huang[3†], Long-Qing Chen[4], Shenglin Jiang[1], Qing Wang[4†]

Although ferroelectric materials exhibit large pyroelectric coefficients, their pyroelectric figures of merit (FOMs) are severely limited by their high dielectric constants because of the inverse relationship between FOMs and dielectric constant. Here, we report the molecular ferroelectric [Hdabco]ClO_4 and [Hdabco]BF_4 (dabco = diazabicyclo[2.2.2]octane) exhibiting improper ferroelectric behavior and pyroelectric FOMs outperforming the current ferroelectrics. Concurrently, the improper molecular ferroelectrics have pyroelectric coefficients that are more than one order of magnitude greater than the state-of-the-art pyroelectric $Pb(Mg_{1/3}Nb_{2/3})O_3$-$PbTiO_3$. Our first-principles and thermodynamic calculations show that the strong coupling between the order parameters, i.e., the rotation angle of anions and polarization, is responsible for the colossal pyroelectric coefficient of the molecular ferroelectrics. Along with the facile preparation and self-poling features, the improper molecular ferroelectrics hold great promise for high-performance pyroelectric devices.

INTRODUCTION

The pyroelectric effect refers to the polarization change of polar materials in response to the variation in temperature and is used in a wide variety of applications ranging from infrared (IR) detection to thermal imaging and energy harvesting (*1*, *2*). The typical pyroelectric materials are ferroelectric single crystals, ceramics, and polymers, such as triglycine sulfate (TGS), lithium tantalate ($LiTaO_3$), lead zirconate titanate [$PbZrTiO_3$ (PZT)], lead magnesium niobate lead titanate [$Pb(Mg_{1/3}Nb_{2/3})O_3$-$PbTiO_3$ (PMN-PT)], and poly(vinylidene fluoride) (PVDF), which have large pyroelectric coefficients (p) arising from the variation of their spontaneous polarization (P_S) with temperature (T), i.e., $|\partial P_S/\partial T|$ (*1*, *3*–*5*).

Several figures of merit (FOMs) have been formulated for pyroelectric materials to evaluate their relative potentials for a number of different applications. For example, for pyroelectric sensors, the FOMs are voltage responsivity $F_V = p/(\varepsilon_0\varepsilon_r c_V)$ and detectivity $F_D = p/[c_V(\varepsilon_0\varepsilon_r \tan\delta)^{1/2}]$, where ε_0, ε_r, c_V, and $\tan\delta$ are the vacuum permittivity, dielectric constant, volumetric heat capacity, and loss tangent, respectively (*1*, *6*). F_V denotes the maximum pyroelectric voltage for a given energy input, while F_D characterizes the ability of detectors to sense weak signals that compete with noises. For pyroelectric energy harvesting, the FOMs are $F_E = p^2/(\varepsilon_0\varepsilon_r)$ and $F_{EN} = p^2T_h/(\varepsilon_0\varepsilon_r c_V)$ (also termed as the electrothermal coupling factor k^2, where T_h is the maximum temperature in the thermal cycle), which represent the amount and efficiency of electric power converted from a given thermal energy input, respectively (*1*, *6*–*8*). Therefore, to achieve high pyroelectric FOMs and factors, it necessitates that pyroelectric materials have simultaneously a high pyroelectric coefficient and a low dielectric constant.

To improve the pyroelectric FOMs, existing approaches have mainly been focused on the structural modification of ferroelectric materials to attain high pyroelectric coefficients (*1*). For example, by varying the $PbTiO_3$ content, the pyroelectric coefficient of PMN-PT reaches the maximum value of 3000 to 5000 $\mu C\ m^{-2}\ K^{-1}$ near the rhombohedral-tetragonal phase transition (*4*). The addition of 15% Sr into $Ba_{0.85}Ca_{0.15}Zr_{0.1}Ti_{0.9}O_3$ (BCZT) ceramic increases the polarization from 16 to 25 $\mu C\ cm^{-2}$ and, consequently, the pyroelectric coefficient from 700 to 1400 $\mu C\ m^{-2}\ K^{-1}$ (*9*). However, the improvement in the pyroelectric coefficient of ferroelectric materials is generally accompanied by an increase in the dielectric constant (note S1), thus imposing a fundamental limit on the magnitude of the pyroelectric FOMs (*10*).

The unique characteristics of improper ferroelectricity offer the potential for overcoming this fundamental limitation (*11*). Contrary to proper ferroelectric whose primary order parameter is polarization, the polarization of improper ferroelectric is a secondary order parameter that develops following the primary order parameter (*12*–*14*). In improper ferroelectrics, the dielectric constant remains low even close to the phase transition temperature, which is usually more than one to two orders of magnitude lower than those of proper ones (*4*, *9*, *15*). The low dielectric constant of improper ferroelectrics is thus conducive to large pyroelectric FOMs. Relatively high pyroelectric FOMs have been demonstrated in improper ferroelectric dicalcium-lead-propionate [$Ca_2Pb(CH_3CH_2COO)_6$ (DLP)] and iron-iodine-boracite [$FeB_7O_{13}I$ (TMO)] stemming from their relatively low dielectric constant of 4 to 13 (*16*). A favorable electrothermal coupling factor has been revealed in stuffed aluminate sodalite [$(Ca_{0.84}Sr_{0.16})_8[AlO_2]_{12}(MoO_4)_2$, CSAM-16] for thermal energy harvesting (*7*, *17*). Nevertheless, the pyroelectric coefficients of DLP and TMO, for example, are ~60 and ~ 80 $\mu C\ m^{-2}\ K^{-1}$, respectively, which are vastly inferior to those of PMN-PT (3000 to 5000 $\mu C\ m^{-2}\ K^{-1}$) and PZT (210 $\mu C\ m^{-2}\ K^{-1}$) (*4*, *18*). This is likely due to the nature of second-order phase transitions in these improper ferroelectric, in

[1]School of Optical and Electronic Information, and Wuhan National Laboratory for Optoelectronics, Huazhong University of Science and Technology, Wuhan, Hubei, China. [2]School of Aerospace Engineering, Beijing Institute of Technology, Beijing, China. [3]School of Materials Science and Engineering, Beijing Institute of Technology, Beijing, China. [4]Department of Materials Science and Engineering, Pennsylvania State University, University Park, PA 16802, USA. [5]Institute of Physics, Chinese Academy of Sciences, Beijing, China. [6]Hubei Key Laboratory of Ferro- & Piezoelectric Materials and Devices, Faculty of Physics and Electronic Science, Hubei University, Wuhan, Hubei, China.
*These authors contributed equally to this work.
†Corresponding author. Email: zhanggz@hust.edu.cn (G.Z.); hongjw@bit.edu.cn (J.W.); hbhuang@ustb.edu.cn (H.H.); wang@matse.psu.edu (Q.W.)

which the polarization decreases slowly with an increasing temperature around the phase transition temperature. The improper ferroelectric di-*n*-butylaminium trifluoroacetate, which exhibits a first-order phase transition, presents a large pyroelectric coefficient of 5500 μC m^{-2} K^{-1} and high FOMs of F_V = 0.58 m^2 C^{-1} and $F_D = 1.5 \times 10^{-5}$ $Pa^{-1/2}$ (*19*).

Here, we report improper molecular ferroelectric [Hdabco]ClO_4 and [Hdabco]BF_4 (dabco = diazabicyclo[2.2.2]octane) that have far superior pyroelectric coefficients and FOMs to the current ferroelectric materials. Our first-principles and thermodynamic calculations reveal the decisive role of the coupling between the rotation of $[ClO_4]^-$ anion, the primary order parameter of the improper phase transition, and the polarization, the secondary order parameter, in the pyroelectric responses of the molecular ferroelectrics. Moreover, different from conventional ferroelectrics, [Hdabco]ClO_4 is capable of operating cyclically at the ferroelectric-paraelectric phase transition temperature, i.e., the Curie temperature (T_C), without visible signs of degradation in the pyroelectric coefficient.

RESULTS AND DISCUSSION

X-ray diffraction (XRD) was performed on [Hdabco]ClO_4 to reveal its atomic structures in orthorhombic and tetragonal phases (Fig. 1, fig. S1, and table S1). The crystal structures of [Hdabco]ClO_4 are illustrated in Fig. 1 (C to F). At 303 K, the appearance of the (020), (200), (111) diffraction peaks at 2θ = 18.40°, 19.96°, and 21.34°, respectively (Fig. 1A), manifests the orthorhombic phase of ferroelectric [Hdabco]ClO_4 adopting the noncentrosymmetry $Pm2_1n$ space group (Fig. 1, C and E). The lattice parameters of [Hdabco]ClO_4 extracted from the XRD pattern are a = 8.827 Å, b = 9.714 Å, and c = 5.378 Å. With the increase of temperature, e.g., at 403 K, [Hdabco]ClO_4 is highly disordered and exhibits a tetragonal structure assigned to the centrosymmetric *P4/mmm* space group (Fig. 1, D and F) with lattice parameters of $a = b$ = 6.672 Å and c = 5.369 Å (Fig. 1B and fig. S1). Second-harmonic generation (SHG) was performed to provide further insight into the local symmetry (*19*, *20*). As shown in fig. S2, at temperatures above 378 K, which is the T_C of [Hdabco]ClO_4 determined from dielectric spectroscopy (Fig. 2A), the SHG signal is close to zero, reaffirming the centrosymmetric phase structure of [Hdabco]ClO_4. The symmetry of [Hdabco]ClO_4 is broken as temperature decreases to below 378 K as evidenced by the emergence of the SHG signals (*20*). The differential scanning calorimetry (DSC) profile measured at a heating and cooling scan rate of 1 K min^{-1} shows distinct endothermic and exothermic peaks with a heat hysteresis of 3 K (fig. S3A), which is a clear manifestation of the first-order phase transition (*21*). The heat hysteresis grows more pronounced by increasing the rate of heating and cooling (fig. S3B).

Figure 2A presents the dielectric spectra of [Hdabco]ClO_4 as a function of temperature, in which the dielectric constant step corresponding to the ferroelectric-paraelectric phase transition appears at 378 K. [Hdabco]ClO_4 shows a bistable dielectric constant spanning the ferroelectric and paraelectric phases with relative permittivities of 9 and 18, respectively, measured at 1 kHz, which is distinctly different from proper ferroelectrics with a dielectric constant peak obeying the Curie-Weiss law around the Curie temperature (*22*–*24*). Meanwhile, [Hdabco]ClO_4 has a loss tangent of 0.001 before the T_C and 0.08, which is comparable to that of PZT thin films (*18*), after the T_C (Fig. 2A).

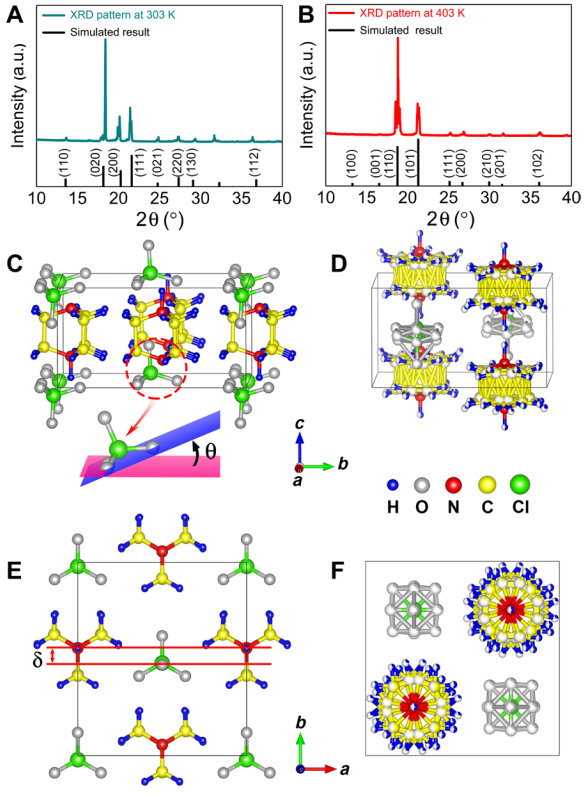

Fig. 1. XRD patterns and molecular structure of [Hdabco]ClO_4. XRD patterns of (**A**) orthorhombic and (**B**) tetragonal phases of [Hdabco]ClO_4 along with the simulated results. a.u., arbitrary units. The molecular structures of (**C** and **E**) orthorhombic and (**D** and **F**) tetrahedral phases viewed along the different directions. The dihedral angle θ is the angle between the plane composed of three oxygen atoms and the *ab* plane, and the ionic displacement δ is the one between the centers of $[Hdabco]^+$ cation and $[ClO_4]^-$ anion along the *b* axis.

The polarization-field (*P-E*) loops of [Hdabco]ClO_4 were recorded to evaluate its ferroelectricity. As shown in Fig. 2B and fig. S4, at ambient temperature, a saturated ferroelectric hysteresis loop with a polarization of ~6 μC cm^{-2} and a coercive field of 75 kV cm^{-1} is attained using the Sawyer-Tower circuit. The ferroelectric nature of [Hdabco]ClO_4 is further confirmed by the current–electric field (*I-E*) curve. As shown in fig. S4, the current is maximized exactly at the coercive field instead of the maximum electric field, which is known as a direct evidence of ferroelectricity as the current peak is generated by the dipole reversal rather than electrical conductivity. The *P-E* loops of [Hdabco]ClO_4 at different temperatures are shown in Fig. 2B. The minor change of the *P-E* loops measured at temperatures below 378 K indicates the ferroelectric stability of orthorhombic [Hdabco]ClO_4. When the temperature exceeds 378 K, the near-square hysteresis loops are transformed into slim linear loops, accompanied by a dramatic decrease in polarization, owing to the formation of the paraelectric phase. As indicated by the light blue area in Fig. 2C, the spontaneous polarization of [Hdabco]ClO_4 shows an abrupt change to nearly zero around the T_C, suggesting an extremely high $|\partial P_S/\partial T|$ and a giant pyroelectric coefficient of [Hdabco]ClO_4.

The pyroelectric measurements were carried out using the Byer-Roundy method. The maximum pyroelectric coefficient of 48,000 μC m^{-2} K^{-1} is achieved in [Hdabco]ClO_4 at the T_C of 378 K (Fig. 2D), which far exceeds the state-of-the-art pyroelectric materials,

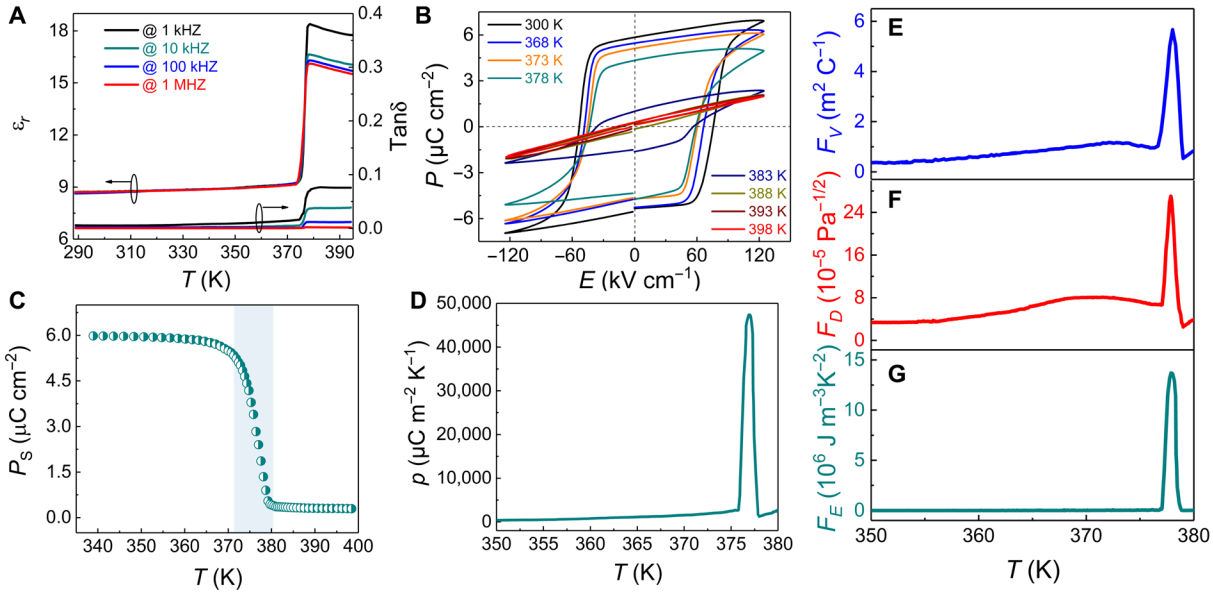

Fig. 2. The dielectric, ferroelectric, and pyroelectric properties of [Hdabco]ClO_4. (**A**) Dielectric constant (ε_r) and loss tangent (tanδ) of [Hdabco]ClO_4 as a function of temperature. (**B**) Polarization-field (*P-E*) loops of [Hdabco]ClO_4 measured at 100 Hz and different temperatures. (**C**) Spontaneous polarization (P_S) as a function of temperature. A marked drop is observed at 378 K, corresponding to the Curie phase transition. (**D**) Temperature-dependent pyroelectric coefficient (*p*). (**E**) Voltage responsivity (F_V). (**F**) Detectivity (F_D). (**G**) FOM of energy harvesting (F_E).

e.g., about 16 and 50 times greater than the typical proper pyroelectric materials such as PMN-PT and barium zirconate titanate (BZT), respectively, more than three orders of magnitude higher than those of ferroelectric polymers, and 8 times larger than the newly developed improper dielectric di-*n*-butylaminium trifluoroacetate (Fig. 3 and Table 1) (*1*, *4*, *9*, *19*). Notably, as shown in Fig. 3, the colossal pyroelectric coefficient of [Hdabco]ClO_4 is coupled with a dielectric constant that is orders of magnitude lower than those of PMN-0.13PT (>3100) and PZT (>375). This is in stark contrast to the existing pyroelectric materials showing the positive relationship between the pyroelectric coefficient and the dielectric constant (*10*). Consequently, [Hdabco]ClO_4 exhibits the state-of-the-art FOMs, i.e., F_V of 5.58 m^2 C^{-1}, F_D of 25.2×10^{-5} Pa$^{-1/2}$, F_E of 1.36×10^7 J m^{-3} K^{-2}, and F_{EN} of 20.6% around T_C (Fig. 2, E to G, and Table 1), far outperforming the current proper and improper ferroelectrics as compared in Table 1. At room temperature, although the pyroelectric coefficients of [Hdabco]ClO_4 and [Hdabco]BF_4 are inferior to those of most proper ferroelectrics, the FOMs of these two improper ferroelectrics are still comparable to those of proper ferroelectrics because of their small and stable dielectric constants.

The process of poling using a sufficiently large electric field is required for traditional ferroelectric materials to align the electric dipoles for macroscopic pyroelectric responses. In contrast, high pyroelectric signals in [Hdabco]ClO_4 are obtained without poling due to the spontaneous formation of the orientated polarization during the growth of [Hdabco]ClO_4, which is validated by piezoresponse force microscopy (PFM). Figure S5 presents the domain orientations at four random places of a fresh [Hdabco]ClO_4 film. It is seen that all the domains direct toward the same direction, indicating that the dipoles spontaneously align along the same direction during the deposition process. The self-poling field estimated from the *P-E* loops is ~12 kV cm^{-1}, which is about 20% of the coercive field (fig. S6). Because of the self-poling effect, when operating cyclically across the T_C, no obvious decay in the pyroelectric coefficient was observed in [Hdabco]ClO_4, as shown in fig. S7. On the contrary, most conventional ferroelectric materials lose their pyroelectric activity at temperatures above the T_C and are unable to regain pyroelectricity even after the temperature drops below the T_C unless they are repoled under an applied electric field. The self-poling effect can be counteracted by applying a reversed electric field whose magnitude is equal to the coercive field with the self-poling effect (E_C^+ in fig. S6A). As shown in fig. S6B, the offset of the *P-E* loop decreases notably after poling with the reversed field. The pyroelectric response of the sample poled with the reversed field is only about one-eighth those of the unpoled specimen (fig. S8).

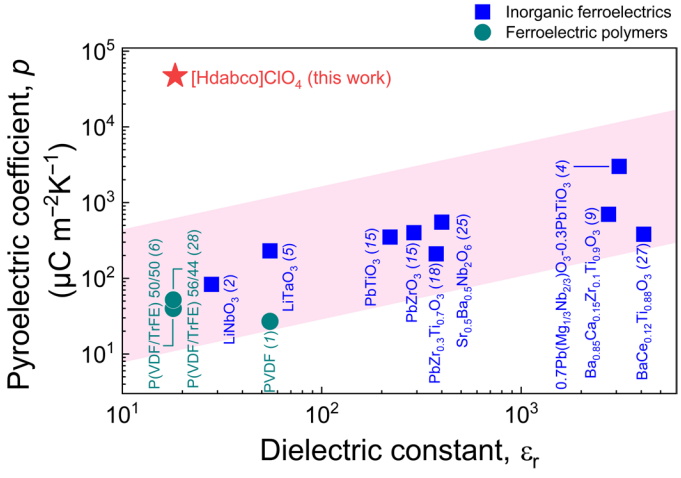

Fig. 3. The pyroelectric coefficients and dielectric constants of pyroelectric materials. $PbZrO_3$ (*15*), $PbTiO_3$ (*15*), $PbZr_{0.3}Ti_{0.7}O_3$ (*18*), $0.7Pb(Mg_{1/3}Nb_{2/3})O_3$–$0.3PbTiO_3$ (*4*), $LiTaO_3$ (*5*), $LiNbO_3$ (*2*), $Sr_{0.5}Ba_{0.5}Nb_2O_6$ (*45*), $BaCe_{0.12}Ti_{0.88}O_3$ (*46*), $Ba_{0.85}Ca_{0.15}Zr_{0.1}Ti_{0.9}O_3$ (*9*), PVDF (*1*), P(VDF/TrFE)50/50 (*6*), and P(VDF/TrFE)56/44 (*47*).

Table 1. The pyroelectric coefficients and FOMs of ferroelectric materials. The units of temperature, p, c_V, F_V, F_D, F_E, and F_{EN} are K, μC m^{-2} K^{-1}, MJ m^{-3} K^{-1}, m^2 C^{-1}, 10^{-5} Pa$^{-1/2}$, J m^{-3} K^{-2}, and %, respectively. RT, room temperature.

	Materials	Temperature	p	c_V	ε_r	Tanδ	F_V	F_D	F_E	F_{EN}	References
Proper ferroelectrics	$PbZrO_3$	~RT	400	2.5	290	0.003	0.062	5.8	62.3	0.74	(*15*)
		~T_C					–				
	$PbTiO_3$	~RT	350	2.2	220	0.001	0.082	11.4	62.9	0.85	(*15*, *48*)
		~T_C					–				
	$Pb(Zr,Ti)O_3$	~RT	211	3.15	365	0.089	0.021	0.4	13.8	0.13	(*18*)
		~T_C					–				
	$0.7Pb(Mg_{1/3}Nb_{2/3})O_3$-$0.3PbTiO_3$	~RT	1,200	2.7	1800	0.01	0.028	3.5	90.4	1	(*4*, *49*, *50*)
		~T_C	3,000	–	17,000	0.08	0.007	1	59.8	–	
	$LiTaO_3$	~RT	230	0.75	55	–	0.630	–	108.6	4.4	(*5*, *51*)
		~T_C	9,800	1.02	2600	–	–	–	4172	–	
	$LiNbO_3$	~RT	83	2.32	28	–	0.144	–	27.8	0.4	(*2*, *52*)
		~T_C					–				
	$Sr_{0.5}Ba_{0.5}Nb_2O_6$	~RT	550	2.34	400	0.003	0.066	7.2	85.4	1.1	(*45*, *53*, *54*)
		~T_C	900	–	3600	38	0.012	0.04	25.4	–	
	$94.6Na_{0.5}Bi_{0.5}TiO_3$-$5.4BaTiO_3$	~RT	588	2.89	279	0.019	0.082	3	140	1.4	(*55*, *56*)
		~T_C					–				
	$BaCe_{0.12}Ti_{0.88}O_3$	~RT	381	2.09	4117	0.055	0.005	0.4	4	0.06	(*46*, *57*)
		~T_C	8,900	–	13,300	0.014	0.036	10.5	672.7	–	
	$Ba_{0.85}Ca_{0.15}Zr_{0.1}Ti_{0.9}O_3$	~RT	700	2.33	2743	0.023	0.012	1.3	20.2	0.26	(*9*, *58*)
		~T_C	980	–	5500	0.059	0.009	0.79	19.7	–	
	Triglycinesulfate (TGS)	~RT	400	2.6	38	0.018	0.457	6.25	475.6	5.5	(*3*)
		~T_C	550	–	55	0.025	0.434	6.06	621.2	–	
	Deuterated triglycinesulfate (DTGS)	~RT	350	2.4	31	0.018	0.531	6.65	446.3	5.64	(*3*)
		~T_C	550	–	43	0.02	0.602	8.31	794.5	–	
	PVDF	~RT	12	2.6	8	0.03	0.065	0.35	2.03	0.023	(*1*)
		~T_C					–				
	P(VDF/TrFE)	~RT	52	2.2	18	0.053	0.148	0.81	16.97	0.23	(*47*, *59*)
		~T_C	142	2.2	33	0.04	0.221	1.89	69.01	1.03	
Improper ferroelectrics	$Ca_2Pb(CH_3CH_2COO)_6$ (DLP)	~RT					–				(*16*)
		~T_C	60	–	8	–	0.54	–	50.8		
	$FeB_7O_{13}I$ (TMO)	~RT					–				(*16*)
		~T_C	80	–	13	–	0.58	–	55.6		
	Di-*n*-butylaminium trifluoroacetate	~RT					–				(*19*)
		~T_C	5,500	–	9.3	0.018	0.58	–	3.7×10^5		
	$(Ca_{0.84}Sr_{0.16})_8[AlO_2]_{12}(MoO_4)_2$	~RT	1	2.78	9.7	0.01	0.004	0.04	0.012	1.2×10^{-4}	(*7*)
		~T_C	120	–	12.4	0.03	0.39	2.38	131.16	2.09	
	$[Hdabco]ClO_4$	~RT	83	1.23	8.7	0.005	0.88	10.9	89.43	2.2	This work
		~T_C	48,000	51.8	18.4	0.08	5.58	25.2	1.36×10^7	20.6	
	$[Hdabco]BF_4$	~RT	81	2.14	16.5	0.003	0.26	5.7	44.91	0.63	
		~T_C	38,200	18.1	38.5	0.09	6.19	38.1	2.73×10^6	59.9	

To understand the experimental results of $[Hdabco]ClO_4$, we calculated the static dielectric constant (ε_{std}), including the electronic (ε_{ele}) and ionic (ε_{ion}) contributions, and Born effective charges (Z^*) using the first-principles method, and the results are summarized in tables S2 and S3. The calculated ε_{std} of $[Hdabco]ClO_4$ are $\varepsilon_{std}^{xx} = 7.76$, $\varepsilon_{std}^{yy} = 3.35$, and $\varepsilon_{std}^{zz} = 4.05$, which are comparable to the experimental values at room temperature (Fig. 2A). For the purpose of comparison, the corresponding theoretical values of a typical organic-inorganic

compound $CH_3NH_3PbI_3$ were computed (table S3). [Hdabco]ClO_4 only contains light elements (Cl and O), leading to its higher IR-active phonon mode frequencies (ω_λ) than those of $CH_3NH_3PbI_3$ with heavier elements (Pb and I). As ε_{ion} is inversely proportional to the frequency of the λ^{th} ω_λ (*25*), ε_{ion} of [Hdabco]ClO_4 is smaller than that of $CH_3NH_3PbI_3$. Because the ionic part contributes mostly to the ε_{std}, the small ε_{ion} is responsible for the lower ε_{std} of [Hdabco]ClO_4 compared to $CH_3NH_3PbI_3$ (*26*). Along with a relatively small Z^* (table S2), [Hdabco]ClO_4 therefore has a low dielectric constant.

We performed the first-principles calculations and thermodynamics simulations to unveil the origin of the ultrahigh pyroelectric coefficient found in [Hdabco]ClO_4. The comparison of the polar and nonpolar structures of [Hdabco]ClO_4 reveals two apparent differences: the rotation of $[ClO_4]^-$ (θ; Fig. 1C) and the columnar shift (polarization) of the centers of $[Hdabco]^+$ and $[ClO_4]^-$ groups along the *b* direction (δ; Fig. 1E). We then chose θ as the primary order parameter and δ as the secondary parameter corresponding to polarization in the Landau-Devonshire theory, which is also in line with the coupling scheme of different distortions to induce improper ferroelectricity in molecular materials (*27*–*29*). The rotation of $[ClO_4]^-$ versus energy was calculated to provide the fitting parameters for thermodynamics analysis using the Landau-Devonshire theory based on the spontaneous polarization-temperature (P_S-T) curves from our experimental results. The general formula of free energy for improper ferroelectrics is given by $G = \alpha_1\theta^2 + \alpha_{11}\theta^4 + \alpha_{111}\theta^6 + \beta_1P^2 + \gamma_1\theta P + \gamma_2\theta^2P^2$ (*30*–*32*), where α_1, α_{11}, α_{111}, and β_1 are the Landau coefficients; θ is the primary order parameter; P is the polarization; $\gamma_1\theta P$ and $\gamma_2\theta^2P^2$ are respectively the linear and nonlinear coupling between θ and P in terms of polarization; and γ_1 and γ_2 represent the coupling coefficients, respectively. The values of Landau and coupling coefficients are summarized in table S4. It is found from the thermodynamic calculation that the P_S decreases significantly from ~5 μC cm^{-2} to zero and shows the first-order transition near the T_C (Fig. 4A). The calculated P_S-T curve is in good agreement with the experimental result, which verifies our calculations. The calculated pyroelectric coefficient of about 46,700 μC cm^{-2} K^{-1} (table S5) also agrees well with the experimental result.

For comparison, we prepared and characterized [Hdabco]BF_4 with the same lattice structure as [Hdabco]ClO_4 (*20*), which also shows a bistable dielectric behavior at the Curie transition (fig. S7B). The pyroelectric coefficient of [Hdabco]BF_4 measured by the Byer-Roundy method is 38,200 μC m^{-2} K^{-1}, which is less than that of [Hdabco]ClO_4 (fig. S7D). We calculated the P_S-T curve of [Hdabco]BF_4 (Fig. 4A) using the same thermodynamic scheme performed on [Hdabco]ClO_4, and the calculated pyroelectric coefficient is 37,600 μC m^{-2} K^{-1} (table S5).

The high pyroelectric coefficients of [Hdabco]ClO_4 and [Hdabco]BF_4 are obtained because the temperature dependence of polarization is dominated by the primary order parameter θ in improper ferroelectrics. As exhibited in Fig. 4B, according to the thermodynamic calculation, it can be seen that the P_S is strongly dependent on the primary order parameter θ (*21*, *33*). As the θ for the materials is a function of temperature, the pyroelectric coefficient of the improper ferroelectrics is determined by the coupling effect between the primary order parameter and the polarization. As listed in table S5, a larger slope of the P-θ curve of [Hdabco]ClO_4 thus results in a higher pyroelectric coefficient in comparison to [Hdabco]BF_4. Therefore, the high pyroelectric coefficients of [Hdabco]ClO_4 and [Hdabco]BF_4 are attributable to the strong coupling effect between the primary order parameter θ and the secondary order parameter polarization.

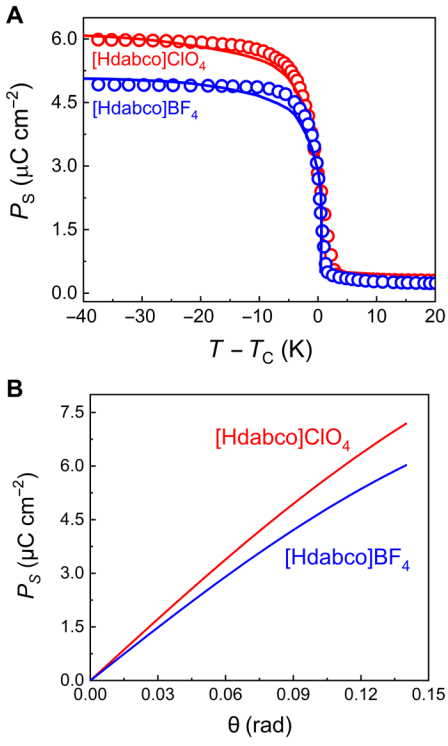

Fig. 4. The experimental and calculated spontaneous polarization of [Hdabco]ClO_4 and [Hdabco]BF_4. (**A**) Comparison of the experimental and simulated temperature-dependent P_S of [Hdabco]ClO_4 and [Hdabco]BF_4. The plots are the experimental data, and the solid lines are the calculated results. (**B**) Relation between the spontaneous polarization of [Hdabco]ClO_4 and [Hdabco]BF_4 and the rotation angle. The stepper slop of [Hdabco]ClO_4 indicates its stronger coupling between the polarization and θ than that of [Hdabco]BF_4.

Compared to the proper ferroelectric, improper ferroelectric remains largely unexplored for technological applications, although their structures and properties are of significant fundamental scientific importance. In this work, we demonstrate an efficient route to overcoming the fundamental limitation of proper ferroelectrics and significant improvement of the pyroelectric FOMs by capitalizing on the unique features of improper ferroelectric. The exceptional combination of an ultrahigh pyroelectric constant and a low dielectric constant in the improper molecular ferroelectric addresses the "high pyroelectric coefficient associated with large dielectric constant" dilemma in the current ferroelectric materials, providing a new degree of freedom in the design of pyroelectric materials that is not accessible to proper ferroelectrics. We observe unprecedentedly large pyroelectric coefficient and the pyroelectric FOMs from improper molecular ferroelectric [Hdabco]ClO_4 and [Hdabco]BF_4. We explain the observed dielectric and pyroelectric behavior using first-principles calculations and thermodynamics simulations and reveal the impact of the coupling of the primary order parameter and the secondary order parameter on the pyroelectric coefficient of the improper molecular ferroelectric. Moreover, our materials are found to retain their high pyroelectric responses when operating cyclically across the T_C. The unexpectedly high pyroelectric performance and unconventional mechanisms of improper ferroelectrics may provide

a new paradigm for applying molecular design guidelines to fundamentally enable their technological applications. The high pyroelectric coefficients reported herein are observed in a relatively narrow temperature range near the Curie transition (Fig. 2 and figs. S9 and S10) because of the first-order phase transition nature. Achieving high pyroelectric coefficients in a wide temperature range represents a critical direction for future research in the field. It is anticipated that the significant breakthrough can be realized in the molecular ferroelectrics given their design flexibility and structure tunability (*34*, *35*).

MATERIALS AND METHODS

Sample preparation

All reagents and solvents were commercial and implemented without further purification. 1,4-Diazabicyclooctane triethylenediamine (Dabco) (98%, Aladdin) and perchloric acid ($HClO_4$) (analytically pure, Sinopharm Chemical Reagent) were dissolved in deionized water with a ratio of 1:1 and stirred for 30 min. [Hdabco]ClO_4 was precipitated out with the slow evaporation of the solution. The collected [Hdabco]ClO_4 powder was then dissolved in deionized water to form a clear solution (100 mg ml^{-1}). Subsequently, the solution was cast onto an indium tin oxide glass, and a layer of [Hdabco]ClO_4 film was deposited on the substrate after solvent evaporation. The [Hdabco]BF_4 crystal was synthesized with equimolar dabco and fluoboric acid (HBF_4). The synthesis process is the same as that of [Hdabco]ClO_4.

Sample characterization

The information of phase and crystalline structure was analyzed at different temperatures by an XRD with a Cu Kα radiation (Empyrean, PANalytical B.V., The Netherlands). DSC was conducted by using a DSC-Q2000 differential scanning calorimeter (TA Instrument Co., DE, USA). PFM was performed with a Smena P47H (NT-MDT Co., Moscow, Russia). SHG measurement was carried out to explore the nonlinear optical property of the materials. The incident laser is produced by a Ti:sapphire oscillator with a central wavelength of 800 nm, a pulse duration of 120 fs, and a repetition of 82 MHz. Au top electrodes with a diameter of 1 mm were sputtered by an ion sputter coater (SBC-12, KYKY, China) for the electrical measurements. *P-E* loops were collected using the Polarization Loop Test System (CPE1601, PolyK Technologies, State College, PA, USA) with the Sawyer-Tower circuit. Dielectric spectra were acquired over a broad temperature range using the Dielectric Test System (PK-CPT1705, PolyK Technologies, State College, PA, USA). Pyroelectric signals of the samples were collected by the Pyroelectric Test System (PK-SPIV17T, PolyK Technologies, State College, PA, USA) on the basis of the Byer-Roundy method (*36*). The heating rate for the measurements of dielectric constants and losses, and pyroelectric coefficients as a function of temperature is 2 K min^{-1}.

Theory modeling

First-principles calculations

Density functional theory (DFT) calculations were performed using the projector-augmented wave (PAW) method as implemented in the Vienna Ab initio Simulation Package (VASP) 5.4 code (*37*, *38*). The generalized gradient approximation (GGA) Perdew-Burke-Ernzerhof (PBE) functional was chosen for structural relaxations and total energy calculations (*39*). The plane-wave cutoff energy was set to 500 eV. The Γ-centered *k*-point meshes with *k*-spacing of ~0.2 $Å^{-1}$ were used for sampling the Brillouin zone (*40*). The lattice parameters were fixed to the experimental values, and only atomic positions were allowed to relax until the force on each atom is smaller than 0.01 eV $Å^{-1}$. ε_{std} and Born effective charges were calculated on the basis of the density functional perturbation theory (DFPT) method (*41*, *42*). The coefficients for the Landau polynomial are obtained by fitting the calculated total energies as a function of the magnitude of the order parameters for the configurations corresponding to displacement patterns for each individual mode or combination of modes.

Thermodynamic calculations

The total free energy of improper ferroelectric materials generally can be expressed by

$$G = \alpha_1\theta^2 + \alpha_{11}\theta^4 + \alpha_{111}\theta^6 + \beta_1 P^2 + \gamma_1\theta P + \gamma_2\theta^2 P^2 \quad (1)$$

where θ is the primary order parameter. It should be noted that α_1, α_{11}, α_{111}, β_1, γ_1, and γ_2 are the thermodynamic potential coefficients, all of which are temperature independents except α_1 and α_{111}, $\alpha_1 = \alpha_0(T - T_C)$ and $\alpha_{111} = a_{111}(T)$ for temperatures above the Curie-Weiss temperature, whereas quantum mechanical contributions were considered for low temperatures (expressions at the end of this section). T, T_C, and P are the temperature, Curie-Weiss temperature, and polarization, respectively. P_s can be obtained from

$$0 = \left(\frac{\partial G}{\partial P}\right)_{P=P_s} = 2\beta_1 P_s + \gamma_1\theta + 2\gamma_2\theta^2 P_s \quad (2)$$

$$0 = \left(\frac{\partial G}{\partial \theta}\right)_{\theta=\theta_s} = 2\alpha_1\theta_s + 4\alpha_{11}{\theta_s}^3 + 6\alpha_{111}{\theta_s}^5 + \gamma_1 P + 2\gamma_2\theta_s P^2 \quad (3)$$

differential with the temperature

$$2\alpha_0\theta_s + \gamma_1\frac{dP}{dT} + 4\gamma_2\theta_s P\frac{dP}{dT} = 0 \quad (4)$$

where $p = -\frac{dP}{dT}$

$$p = \frac{2\alpha_0\theta}{\gamma_1 + 4\gamma_2\theta P} \quad (5)$$

The reciprocal susceptibility can be given by

$$\chi = \frac{1}{\varepsilon} = \frac{1}{\varepsilon_r\varepsilon_0} = \left(\frac{\partial^2 G}{\partial P^2}\right)_{P=P_s} = 2\beta_1 + 2\gamma_2\theta^2 \quad (6)$$

$$\frac{p}{\varepsilon} = \frac{4\alpha_0\theta(\beta_1 + \gamma_2\theta^2)}{\gamma_1 + 4\gamma_2\theta P} \quad (7)$$

At a steady state, the variation of energy with order parameters was taken to be zero; therefore, $\frac{\partial G}{\partial P} = 0$ and $\frac{\partial G}{\partial \theta} = 0$, and we had

$$0 = 2\beta_1 P + \gamma_1\theta + 2\gamma_2\theta^2 P \quad (8)$$

$$0 = 2\alpha_1\theta + 4\alpha_{11}\theta^3 + 6\alpha_{111}\theta^5 + \gamma_1 P + 2\gamma_2\theta P^2 \quad (9)$$

Combining the above two equations and eliminating the primary order parameter θ, we got

$$T - T_C = \frac{4\alpha_{11}\left(\frac{-\gamma_1 \pm \sqrt{\gamma_1^2 - 16\gamma_2\beta_1 P^2}}{4\gamma_2 P}\right)^3 + 6\alpha_{111}\left(\frac{-\gamma_1 \pm \sqrt{\gamma_1^2 - 16\gamma_2\beta_1 P^2}}{4\gamma_2 P}\right)^5 + \gamma_1 P + 2\gamma_2\left(\frac{-\gamma_1 \pm \sqrt{\gamma_1^2 - 16\gamma_2\beta_1 P^2}}{4\gamma_2 P}\right)P^2}{-2\alpha_0\left(\frac{-\gamma_1 \pm \sqrt{\gamma_1^2 - 16\gamma_2\beta_1 P^2}}{4\gamma_2 P}\right)} \quad (10)$$

Experimental P_S-T data were fitted on the above equation to derive the values of the coefficients α_0, α_{11}, α_{111}, β_1, γ_1, and γ_2, with the assumption that α_0 and α_{11} depend on environmental factors/experimental conditions. α_{111} is considered to be temperature dependent, and low-temperature quantum effects were incorporated in α_1 and α_{111} in the calculation (*43*). Therefore, at temperatures above T_C, α_{111} is given as

$$\alpha_{111} = a_{111}(T) \tag{11}$$

whereas at temperatures below T_C, α_1 and α_{111} take the form

$$\alpha_1 = \alpha_0 T_s\left[\coth\left(\frac{T_s}{T}\right) - \coth\left(\frac{T_s}{T_c}\right)\right] \tag{12}$$

$$\alpha_{111} = b_{111} T_s\left[\coth\left(\frac{T_s}{T}\right) - \coth\left(\frac{T_s}{T_c}\right)\right] \tag{13}$$

where T_s is the saturated temperature below which quantum effects become significant; here, we used T_s taken experimentally from KH_2PO_4 crystal with similar order-disorder phase transition (*44*). The extracted coefficients are listed in table S4.

SUPPLEMENTARY MATERIALS

Supplementary material for this article is available at http://advances.sciencemag.org/cgi/content/full/7/5/eabe3068/DC1

REFERENCES AND NOTES

1. R. W. Whatmore, Pyroelectric devices and materials. *Rep. Prog. Phys.* **49**, 1335–1386 (1986).
2. S. B. Lang, Pyroelectricity: From ancient curiosity to modern imaging tool. *Phys. Today* **58**, 31–36 (2005).
3. P. Felix, P. Gamot, P. Lacheau, Y. Raverdy, Pyroelectric, dielectric and thermal properties of TGS, DTGS and TGFB. *Ferroelectrics* **17**, 543–551 (1977).
4. J. H. Park, B. K. Kim, K. H. Song, S. J. Park, Electric-field induced strains and pyroelectric coefficients in lead magnesium niobate-lead titanate solid solutions. *Mater. Res. Bull.* **30**, 435–441 (1995).
5. B. M. Kulwicki, A. Amin, H. R. Beratan, C. M. Hanson, Pyroelectric imaging. *Proc. IEEE Int. Symp. Appl. Ferroelectrics* , 1–10 (1992).
6. S. B. Lang, D. K. Das-Gupta, Chapter 1—Pyroelectricity: Fundamentals and applications, in *Handbook of Advanced Electronic and Photonic Materials and Devices* (Academic Press, 2001), vol. 4, pp. 1–55.
7. T. Wakamatsu, K. Tanabe, I. Terasaki, H. Taniguchi, Improper ferroelectrics as high-efficiency energy conversion materials. *Phys. Status Solidi RRL* **11**, 1770324 (2017).
8. G. Sebald, E. Lefeuvre, D. Guyomar, Pyroelectric energy conversion: Optimization principles. *IEEE Trans. Ultrason. Ferroelectr. Freq. Control* **55**, 538–551 (2008).
9. S. Patel, A. Chauhan, R. Vaish, Large pyroelectric figure of merits for Sr-modified $Ba_{0.85}Ca_{0.15}Zr_{0.1}Ti_{0.9}O_3$ ceramics. *Solid State Sci.* **52**, 10–18 (2016).
10. S. T. Liu, J. D. Zook, D. Long, Relationships between pyroelectric and ferroelectric parameters. *Ferroelectrics* **9**, 39–43 (1975).
11. M. E. Lines, A. M. Glass, *Principles and Applications of Ferroelectrics and Related Materials* (Clarendon Press, 1977).
12. E. Bousquet, M. Dawber, N. Stucki, C. Lichtensteiger, P. Hermet, S. Gariglio, J.-M. Triscone, P. Ghosez, Improper ferroelectricity in perovskite oxide artificial superlattices. *Nature* **452**, 732–736 (2008).
13. N. A. Benedek, C. J. Fennie, Hybrid improper ferroelectricity: A mechanism for controllable polarization-magnetization coupling. *Phys. Rev. Lett.* **106**, 107204 (2011).
14. Y. S. Oh, X. Luo, F.-T. Huang, Y. Wang, S.-W. Cheong, Experimental demonstration of hybrid improper ferroelectricity and the presence of abundant charged walls in $(Ca,Sr)_3Ti_2O_7$ crystals. *Nat. Mater.* **14**, 407–413 (2015).
15. D. Luff, R. Lane, K. R. Brown, H. J. Marshallsay, Ferroelectric ceramics with high pyroelectric properties. *Trans. J. Br. Ceram. Soc.* **73**, 251–264 (1974).
16. A. Shaulov, W. A. Smith, G. M. Loiacono, M. I. Bell, Y. H. Tsuo, Improper ferroelectrics for pyroelectric detection of infrared radiation. *Ferroelectrics* **27**, 117–121 (1980).
17. Y. Maeda, T. Wakamatsu, A. Konishi, H. Moriwake, C. Moriyoshi, Y. Kuroiwa, K. Tanabe, I. Terasaki, H. Taniguchi, Improper ferroelectricity in stuffed aluminate sodalites for pyroelectric energy harvesting. *Phys. Rev. Appl.* **7**, 034012 (2017).
18. Q. Zhang, R. W. Whatmore, Sol-gel PZT and Mn-doped PZT thin films for pyroelectric applications. *J. Phys. D Appl. Phys.* **34**, 2296–2301 (2001).
19. Z. Sun, Y. Tang, S. Zhang, C. Ji, T. Chen, J. Luo, Ultrahigh pyroelectric figures of merit associated with distinct bistable dielectric phase transition in a new molecular compound: Di-*n*-butylaminium trifluoroacetate. *Adv. Mater.* **27**, 4795–4801 (2015).
20. Y. Y. Tang, W.-Y. Zhang, P.-F. Li, H.-Y. Ye, Y.-M. You, R.-G. Xiong, Ultrafast polarization switching in a biaxial molecular ferroelectric thin film: $[Hdabco]ClO_4$. *J. Am. Chem. Soc.* **138**, 15784–15789 (2016).
21. M. Szafrański, A. Katrusiak, Thermodynamic behaviour of bistable NH^+–N hydrogen bonds in monosalts of 1,4-diazabicyclo[2.2.2]octane. *Chem. Phys. Lett.* **318**, 427–432 (2000).
22. Y.-M. You, W.-Q. Liao, D. Zhao, H.-Y. Ye, Y. Zhang, Q. Zhou, X. Niu, J. Wang, P.-F. Li, D.-W. Fu, Z. Wang, S. Gao, K. L. Yang, J.-M. Liu, J. Li, Y. Yan, R.-G. Xiong, An organic-inorganic perovskite ferroelectric with large piezoelectric response. *Science* **357**, 306–309 (2017).
23. H.-Y. Ye, Y.-Y. Tang, P.-F. Li, W.-Q. Liao, J.-X. Gao, X.-N. Hua, H. Cai, P.-P. Shi, Y.-M. You, R.-G. Xiong, Metal-free three-dimensional perovskite ferroelectrics. *Science* **361**, 151–155 (2018).
24. D.-W. Fu, H.-L. Cai, Y. Liu, Q. Ye, W. Zhang, Y. Zhang, X.-Y. Chen, G. Giovannetti, M. Capone, J. Li, R.-G. Xiong, Diisopropylammonium bromide is a high-temperature molecular ferroelectric crystal. *Science* **339**, 425–428 (2013).
25. X. Zhao, D. Vanderbilt, First-principles study of structural, vibrational and lattice dielectric properties of hafnium oxide. *Phys. Rev. B* **65**, 233106 (2002).
26. M. H. Du, Efficient carrier transport in halide perovskites: Theoretical perspectives. *J. Mater. Chem. A* **2**, 9091–9098 (2014).
27. H. L. B. Boström, M. S. Senn, A. L. Goodwin, Recipes for improper ferroelectricity in molecular perovskites. *Nat. Commun.* **9**, 2380 (2018).
28. A. Katrusiak, M. Szafrański, Ferroelectricity in **NH···N** hydrogen bonded crystals. *Phys. Rev. Lett.* **82**, 576–579 (1999).
29. A. Budzianowski, A. Katrusiak, M. Szafrański, Anomalous protonic-glass evolution from ordered phase in NH···N hydrogen-bonded $DabcoHBF_4$ ferroelectric. *J. Phys. Chem. B* **112**, 16619–16625 (2008).
30. A. F. Devonshire, XCVI. Theory of barium titanate: Part I. *Philos. Mag.* **40**, 1040–1063 (1949).
31. A. F. Devonshire, CIX. Theory of barium titanate—Part II. *Philos. Mag.* **42**, 1065–1079 (1951).
32. A. Onodera, O. Cynshi, Y. Shiozaki, Landau theory of the ferrielectric phase transition with two order parameters. *J. Phys. C: Solid State Phys.* **18**, 2831–2841 (1985).
33. E. A. Eliseev, A. N. Morozovska, Y. Gu, A. Y. Borisevich, L.-Q. Chen, V. Gopalan, S. V. Kalinin, Conductivity of twin-domain-wall/surface junctions in ferroelastics: Interplay of deformation potential, octahedral rotations, improper ferroelectricity, and flexoelectric coupling. *Phys. Rev. B* **86**, 085416 (2012).
34. J. Long, M. S. Ivanov, V. A. Khomchenko, E. Mamontova, J.-M. Thibaud, J. Rouquette, M. Beaudhuin, D. Granier, R. A. S. Ferreira, L. D. Carlos, B. Donnadieu, M. S. C. Henriques, J. A. Paixão, Y. Guari, J. Larionova, Room temperature magnetoelectric coupling in a molecular ferroelectric ytterbium(III) complex. *Science* **367**, 671–676 (2020).
35. H.-Y. Liu, H.-Y. Zhang, X.-G. Chen, R.-G. Xiong, Molecular design principles for ferroelectrics: Ferroelectrochemistry. *J. Am. Chem. Soc.* **142**, 15205–15218 (2020).
36. R. L. Byer, C. B. Roundy, Pyroelectric coefficient direct measurement technique and application to a nsec response time detector. *Ferroelectrics* **3**, 333–338 (1972).
37. G. Kresse, J. Furthmüller, Efficiency of ab-initio total energy calculations for metals and semiconductors using a plane-wave basis set. *Comput. Mater. Sci.* **6**, 15–50 (1996).
38. G. Kresse, D. Joubert, From ultrasoft pseudopotentials to the projector augmented-wave method. *Phys. Rev. B* **59**, 1758–1775 (1999).
39. J. P. Perdew, K. Burke, M. Ernzerhof, Generalized gradient approximation made simple. *Phys. Rev. Lett.* **77**, 3865–3868 (1996).
40. P. E. Blöchl, O. Jepsen, O. K. Andersen, Improved tetrahedron method for brillouin-zone integrations. *Phys. Rev. B Condens. Matter.* **49**, 16223–16233 (1994).
41. P. Ghosez, J.-P. Michenaud, X. Gonze, Dynamical atomic charges: The case of ABO_3 compounds. *Phys. Rev. B Condens. Matter.* **58**, 6224–6240 (1998).
42. X. Wu, D. Vanderbilt, D. R. Hamann, Systematic treatment of displacements, strains and electric fields in density-functional perturbation theory. *Phys. Rev. B* **72**, 035105 (2005).
43. J.-J. Wang, D. Fortino, B. Wang, X. Zhao, L.-Q. Chen, Extraordinarily large electrocaloric strength of metal-free perovskites. *Adv. Mater.* **32**, e1906224 (2020).
44. G. A. Samara, Vanishing of the ferroelectric and antiferroelectric states in KH_2PO_4-type crystals at high pressure. *Phys. Rev. Lett.* **27**, 103–106 (1971).
45. S. T. Liu, R. B. Maciolek, Rare-earth-modified $Sr_{0.5}Ba_{0.5}Nb_2O_6$ ferroelectric crystals and their applications as infrared detectors. *J. Electron. Mater.* **4**, 91–100 (1975).
46. K. S. Srikanth, R. Vaish, Enhanced electrocaloric, pyroelectric and energy storage performance of $BaCe_xTi_{1-x}O_3$ ceramics. *J. Eur. Ceram. Soc.* **37**, 3927–3933 (2017).

47. M. Dietze, J. Krause, C.-H. Solterbeck, M. Es-Souni, Thick film polymer-ceramic composites for pyroelectric applications. *J. Appl. Phys.* **101**, 054113–054113-7 (2007).
48. K. Iijima, S. Kawashima, I. Ueda, Dielectric and pyroelectric properties of $PbTiO_3$ thin film. *Jpn. J. Appl. Phys.* **24**, 482 (1985).
49. R. Chukka, J. W. Cheah, Z. Chen, P. Yang, S. Shannigrahi, J. Wang, L. Chen, Enhanced cooling capacities of ferroelectric materials at morphotropic phase boundaries. *Appl. Phys. Lett.* **98**, 242902 (2011).
50. G. B. Kim, J. M. Jung, S. W. Choi, Synthesis and ferroelectric properties of Ni-modified $0.7Pb(Mg_{1/3}Nb_{2/3})O_3$-$0.3PbTiO_3$ solid solution system. *Jpn. J. Appl. Phys.* **38**, 5470–5473 (1999).
51. A. M. Glass, Dielectric, thermal, and pyroelectric properties of ferroelectric $LiTaO_3$. *Phys. Rev.* **172**, 564–571 (1968).
52. R. Liu, R. Guo, A. S. Bhalla, L. E. Cross, M. Levy, R. M. Osgood, A. Kumar, H. Bakhru, Dielectric and pyroelectric properties of crystal ion sliced (CIS) $LiNbO_3$ thin film. *Ferroelectrics* **248**, 45–56 (2000).
53. B. Jimenez, C. Alemany, J. Mendiola, E. Maurer, Phase transitions in ferroelectric ceramics of the type $Sr_{0.5}Ba_{0.5}Nb_2O_6$. *J. Phys. Chem. Solid* **46**, 1383–1386 (1985).
54. M. Venet, I. A. Santos, J. A. Eiras, D. Garcia, Potentiality of SBN textured ceramics for pyroelectric applications. *Solid State Ion.* **177**, 589–593 (2006).
55. R. Sun, J. Wang, F. Wang, T.-F. Feng, Y. Li, Z. Chi, X. Zhao, H. Luo, Pyroelectric properties of Mn-doped $94.6Na_{0.5}Bi_{0.5}TiO_3$-$5.4BaTiO_3$ lead-free single crystals. *J. Appl. Phys.* **115**, 074101 (2014).
56. A. M. Balakt, C. P. Shaw, Q. Zhang, The effects of Ba^{2+} content on depolarization temperature and pyroelectric properties of lead-free $0.94Na_{0.5}Bi_{0.5}TiO_3$–$0.06Ba_{1+x}TiO_3$ ceramics. *J. Mater. Sci. Mater. Electron.* **27**, 12947–12954 (2016).
57. S.-M. Zeng, X.-G. Tang, Q.-X. Liu, Y.-P. Jiang, M.-D. Li, W.-H. Li, Z.-H. Tang, Electrocaloric effect and pyroelectric properties in Ce-doped $BaCe_xTi_{1-x}O_3$ ceramics. *J. Alloy. Compd.* **776**, 731–739 (2019).
58. M. Sharma, V. P. Singh, S. Singh, P. Azad, B. Ilahi, N. A. Madhar, Porous $Ba_{0.85}Ca_{0.15}Zr_{0.1}Ti_{0.9}O_3$ ceramics for pyroelectric applications. *J. Electron. Mater.* **47**, 4882–4891 (2018).
59. A. Navid, C. S. Lynch, L. Pilon, Purified and porous poly(vinylidene fluoride-trifluoroethylene) thin films for pyroelectric infrared sensing and energy harvesting. *Smart Mater. Struct.* **19**, 055006 (2010).
60. L. Jin, F. Li, S. J. Zhang, Decoding the fingerprint of ferroelectric loops: comprehension of the 306 material properties and structures. *J. Am. Ceram. Soc.* **97**, 1–27 (2014).
61. A. Katrusiak, M. Ratajczak-Sitarz, E. Grech, Stereochemistry and transformations of $NH\cdots N$ hydrogen bonds Part II. Proton stability in the monosalts of 1,4-diazabicyclo[2.2.2]octane. *J. Mol. Struct.* **474**, 135–141 (1999).
62. A. Katrusiak, Proton dynamics in $NH^+\cdots N$ hydrogen bond in the paraelectric structure of 1,4-diazabicyclo[2.2.2]octane perchlorate. *J. Mol. Struct.* **552**, 159–164 (2000).

Acknowledgments

Funding: G.Z. acknowledges the financial support by the National Natural Science Foundation of China (grant nos. 51972126 and 51772108), the Innovation Fund of WNLO, and the Fundamental Research Funds for the Central Universities (grant nos. 2019KFYRCPY126 and 2018KFYYXJJ052). H.H. is supported by the National Natural Science Foundation of China (grant no. 51972028). J.H. is supported by the National Natural Science Foundation of China (grant no. 11572040) and Beijing Natural Science Foundation (grant no. Z190011). S.J. acknowledges the financial support by the National Natural Science Foundation of China (grant nos. 51972125 and 61675076). K.J. acknowledges the financial supports by the National Natural Science Foundation of China (grant no. 11721404). G.Z. and Y.H. are supported by the Fund of Hubei province key laboratory of ferroelectric materials and devices (K201806). Theoretical calculations were performed using resources of the National Supercomputer Centre in Guangzhou, which was supported by the Special Program for Applied Research on Super Computation of the NSFC-Guangdong Joint Fund (the second phase) under grant number U1501501. We would also like to acknowledge the Analytical and Testing Center of Huazhong University of Science and Technology. **Author contributions:** G.Z., H.H., J.H., J.Z., Q.W., and S.J. conceived and designed the project. W.L., G.Z., and S.J. prepared the samples. W.L., J.W., K.J., Y.H., H.G., Z.W., J.Z., and G.Z. conducted the measurements. G.T. and J.H. performed the first-principles simulations. H.M.J., D.L., H.H., Y.L., and L.-Q.C. performed the thermodynamic analysis. Q.W., G.Z., J.H., H.H., and L.-Q.C. wrote the manuscript with help from all other authors. All authors contributed to the discussion of results. **Competing interests:** The authors declare that they have no competing interests. **Data and materials availability:** All data needed to evaluate the conclusions in the paper are present in the paper and/or the Supplementary Materials. Additional data related to this paper may be requested from the authors.

Submitted 13 August 2020
Accepted 14 December 2020
Published 29 January 2021
10.1126/sciadv.abe3068

Citation: W. Li, G. Tang, G. Zhang, H. M. Jafri, J. Zhou, D. Liu, Y. Liu, J. Wang, K. Jin, Y. Hu, H. Gu, Z. Wang, J. Hong, H. Huang, L.-Q. Chen, S. Jiang, Q. Wang, Improper molecular ferroelectrics with simultaneous ultrahigh pyroelectricity and figures of merit. *Sci. Adv.* **7**, eabe3068 (2021).

Improper molecular ferroelectrics with simultaneous ultrahigh pyroelectricity and figures of merit

Wenru Li, Gang Tang, Guangzu Zhang, Hasnain Mehdi Jafri, Jun Zhou, Di Liu, Yang Liu, Jiesu Wang, Kuijuan Jin, Yongmin Hu, Haoshuang Gu, Zhao Wang, Jiawang Hong, Houbing Huang, Long-Qing Chen, Shenglin Jiang and Qing Wang

Sci Adv **7** (5), eabe3068.
DOI: 10.1126/sciadv.abe3068